Measurement of the neutron spectrum of the ^{51}V(p,n)^{51}Cr reaction at 1585 keV

A. Verdera,* J. Praena, F. Arias de Saavedra, and A. Roldán
University of Granada, Sciences Faculty, Av. Fuentenueva s/n, Granada 18071, Spain

M. Macías, C.L. Fontana, C. Bonaldi, W. Geerts, and S. Oberstedt
European Commission, Joint Research Center, Retieseweg 111, 2440 Geel, Belgium
(Dated: June 30, 2025)

Neutron production by ^{51}V(p,n)^{51}Cr reaction close to the reaction threshold is interesting for its pure production of neutrons at low kiloelectronvolts. In this work, for the first time, the angle-dependent neutron spectrum is measured close to the threshold, particularly at 1585-keV proton energy only 20 keV above the reaction threshold. The experiment was performed at the MONNET facility (JRC-Geel), employing the Time-Of-Flight technique and a thick Vanadium target. The ^{7}Li(p,n)^{7}Be reaction near the threshold was also measured and used as a reference and in a neutron transmission measurement for self-absorption correction. The angular-dependence energy spectra for the ^{51}V(p,n)^{51}Cr has been obtained and the integrated energy spectrum is presented.

Keywords: Neutron production at low keV, Time-Of-Flight technique, astrophysics, BNCT

I. INTRODUCTION

The ^{51}V(p,n)^{51}Cr reaction has been employed as a monoenergetic neutron source in various applications [1–6]. Compared to the ^{7}Li(p,n) reaction, which is the most commonly used reaction for producing kiloelectronvolts neutrons, the greater mass of ^{51}V results in significantly lower neutron energy at the reaction threshold and a smaller variation of energy with angle in the laboratory frame. Therefore, the ^{51}V(p,n)^{51}Cr reaction offers the potential to produce very low-energy epithermal neutrons (few keV) with a modest neutron yield, which could be interesting in fields as nuclear astrophysics or Boron Neutron Capture Therapy (BNCT).

In astrophysics, elements beyond iron are primarily produced through successive neutron-capture reactions and beta decays. In these processes, neutron velocities follow a Maxwell-Boltzmann probability distribution [7, 8] or stellar neutron spectrum. The most important is the slow(s)-process, where two components are identified: the main and weak s-processes.

The modern understanding of the main s-process component is tied to the burning phase that occurs in Asymptotic Giant Branch (AGB) stars [9], where the ^{22}Ne(α,n) reaction is the main neutron source at temperature corresponding to $kT = 30$ keV. This phase primarily produces nuclei with atomic masses between 90 and 209 [10, 11]. Ratynski and Käppeler demonstrated that the ^{7}Li(p,n) near-threshold reaction is able to produce a quasi-stellar neutron spectrum at $kT = 30$ keV [12]. Thus, their method has been extensively used to determine stellar neutron-capture cross-sections by means of the activation technique. At the opposite end, during the ^{13}C(α,n) phase, neutron densities can drop as low as 10^{7} cm^{-3}, with temperatures around $kT = 5$ keV [13]. Therefore, the production of neutrons at a few keV could be useful for directly measuring typical of stellar cross-sections in the ^{13}C(α,n) phase [14]. In this framework, neutron beams produced by means of the ^{51}V(p,n)^{51}Cr near-threshold could be an interesting possibility to mimic the stellar environment in activation measurements.

Another possible application of the ^{51}V(p,n)^{51}Cr reaction is BNCT. The BNCT is an experimental therapy, where neutrons are utilized to deliver a selective cellular dose within, typical a one-day treatment [15]. It administers a ^{10}B compound, preferentially absorbed by tumor cells, which, when irradiated with neutrons, undergoes the ^{10}B(n,α)^{7}Li reaction, irreversibly damaging the cells. Effective BNCT requires sufficient thermal neutrons to reach the tumor, necessitating higher-energy external irradiation and a subsequent neutron moderation. After the recent International Atomic Energy Agency (IAEA) report [16], several constrains on the therapeutic neutron beams, with beam energies below 10 keV, have changed and, in particular, relaxed in terms of neutron flux. The new quality factors and the development of accelerator-based neutron sources instead of nuclear reactors as neutron sources open new possibilities. For instance, we have studied the direct irradiation with neutrons without moderation using a similar reaction as a neutron source, ^{45}Sc(p,n)^{45}Ti [17]. The positive results open new insights in BNCT, for this reason, it is under evaluation for patent. Although, the ^{51}V(p,n)^{51}Cr reaction has a lower neutron yield than ^{45}Sc(p,n)^{45}Ti, it could be compensated with the high-current protons beams of tens of milliampere delivered from the new accelerators already developed for BNCT [16].

The ^{51}V(p,n)^{51}Cr reaction has a threshold of E_p=(1565.28 ± 0.24) keV and a Q-value of (-1534.92 ± 0.24) keV, measured already several times [18–24]. In 1955, Gibbons *et al.* measured the neutron yield for the ^{51}V(p,n)^{51}Cr reaction and identified energy resonances in the energy range E_p=1.56-1.68 MeV [20]. Therefore, this reaction produces a neutron spectra in the keV re-

* averdera@ugr.es

gion with a variety of resonances. Natural vanadium is composed of 99.75% ^{51}V and 0.25% ^{50}V. The ^{51}V(p,n) reaction could be contaminated by the ^{50}V(p,n)^{50}Cr and ^{50}V(p,γ)^{51}Cr reactions. However, the contamination is very low, i.e. less than 0.2% from the ^{50}V(p,n) reaction and no significant γ-ray production [2].

This reaction has been measured by the Time-Of-Flight (TOF) technique on several occasions. One of the first neutron spectrum measurements was performed by Stelson *et al.* [25] at E_p=3.23 and 3.72 MeV. Later, Kneff *et al.* [23] obtained a neutron TOF spectrum for this reaction using a thick target and a proton energy of 1595 keV. Their resulting spectrum reveals a pronounced peak at 6.49 $\pm$ 0.04 keV. Subsequently, Schölermann and Böttger [24] analyzed the resonance structure of the ^{51}V(p,n) cross-section directly above the threshold using TOF measurements. They irradiated a target with a thickness of 50 keV with protons at an energy approximately 50 keV above the reaction threshold. A single discernible peak corresponding to a neutron energy of E_p=(6.44 $\pm$ 0.195) keV was identified. This peak was confirmed by the measurement in Ref. [26] and it is in agreement with Ref. [23].

As for angular-dependence, the only published experiments are those by Ballini *et al.* [27] and by Deconninck *et al.* [28]. First, Ballini *et al.* [27] measured the angular distribution of neutrons from this reaction to the ground state and the first two excited states of ^{51}Cr at a mean proton energy of 4.07 MeV. Later, Deconninick *et al.* [28] described a slow variation of neutron energy with emission angle. To achieve mono-energetic field production, this reaction could be interesting, if it were deployed at a later angle to reach exceptionally low-energies. However, its feasibility depends on the neutron emission rate.

Despite all the mentioned measurements and the extensive nuclear data available for the ^{51}V(p,n)^{51}Cr reaction, the cross-sections reported by different experiments exhibit significant discrepancies. This is particularly evident near the reaction threshold, where the reported values diverge by as much as an order of magnitude [2, 22, 29–36, 38, 39, 41, 42, 45], as depicted in Fig. 1. Additionally, there is a notable lack of data: while a few experiments have reported total neutron and gamma yields, there is a scarcity of experimental information regarding the angular-dependent energy distribution near the reaction threshold.

To address this gap, the present experiment focuses on measuring the angular-dependent energy distribution of the ^{51}V(p,n)^{51}Cr reaction near the threshold. This measurement is conducted using the Time-Of-Flight technique, which allows for a precise determination of the energy distribution as a function of emission angle.

This paper is structured as follows. In Section II, we provide a detailed description of the experimental method, including all the parts of the setup. Section III covers the data analysis along with additional results, including a ^{7}Li(p,n)^{7}Be measurement near the threshold and a transmission measurement through Vanadium.

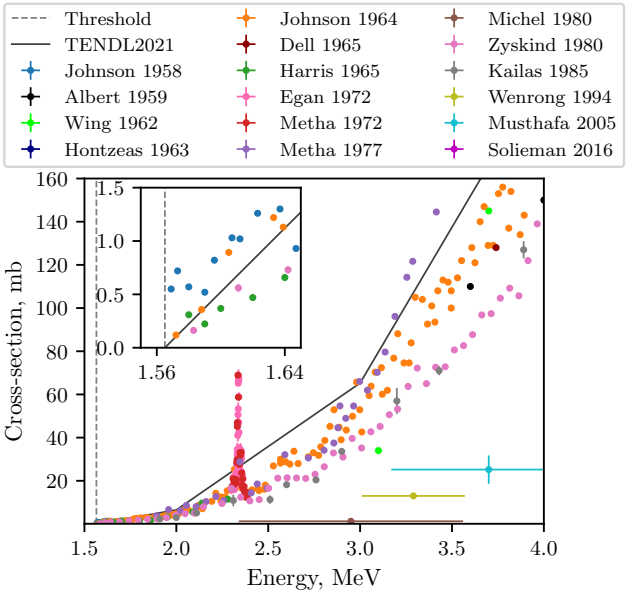

FIG. 1. ^{51}V(p,n)^{51}Cr reaction near-threshold cross-section data: experimental data from Johnson 1958 [29], Albert 1959 [30], Wing 1962 [31], Hontzeas 1963 [32], Johnson 1964 [22], Dell [33], Harris [2], Egan 1972 [34], Metha 1972 [35], Metha 1977 [36], Michel 1980 [37], Zyskind 1980 [38], Kailas 1985 [39], Wenrong 1994 [40], Musthafa 2005 [41] and Solieman [42], taken from EXFOR [43]. Evaluated data from TENDL 2021 [44] and threshold of reaction are also included.

Section IV addresses the results. Finally, the conclusions derived from this research are highlighted in Section V.

II. MATERIALS AND METHODS

The experiment was conducted at the MONNET facility (acronym for MONo-energetic NEutron Tower) at the Joint Research Centre (JRC) in Geel, Belgium EU [46, 47]. This facility consists of a vertical 3.5 MV tandem accelerator capable of generating continuous or pulsed beams of protons or deuterons. Pulsed proton beams with energies from 1.5 to 1.9 MeV and average currents lower than 2 μA were used. The accelerator terminal was calibrated using several resonances by the MONNET local team and tested by us using the ^{51}V(p,n) and ^{7}Li(p,n) reaction at thresholds energies. Possible beam fluctuations were monitored and corrected using a De Pangher precision Long Counter (PLC) detector and a $CeBr_3$ detector. To enable Time-Of-Flight (TOF) measurements, the accelerator operated in pulsed mode with a frequency of 1250 kHz. The chopped and bunched proton beam had a pulse width of 2 ns (FWHM). Figure 2 shows the experimental setup with a proton beam of 1.2 mm diameter. Neutrons were detected by a ^{6}Li-glass detector of 12.7 mm x 57 mm (length x diameter).

For this experiment, two different targets were used:

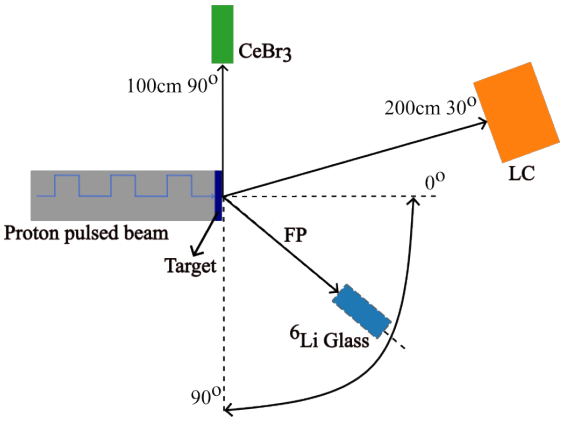

FIG. 2. Diagram of the experimental setup used for our TOF measurements. The ^{6}Li-glass detector is mounted on a movable arm at distance of FP. Two targets were use: LiF onto an Al backing and self-sustained Vanadium foil.

one for the principal vanadium measurement and the other for the additional lithium measurements. The first target assembly consisted of an aluminium cylinder (4.2-cm diameter and 15-cm long) and 1 mm aluminium backing for the lithium fluoride target. A LiF thick target (5-mm diameter and 3.78 mg/cm^2) was prepared by evaporation onto an Al backing. Figure 3 shows the Li target geometry. The second assembly consisted of an aluminium cylinder and a 0.5 mm thick self-supported ^{51}V target, which acted as beam stopper. In both cases, the target assembly was cooled by forced air flow on the external side of the target and the charge at the target was measured.

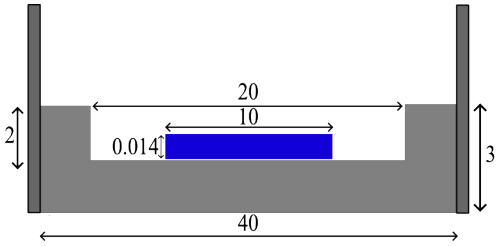

FIG. 3. LiF target detailed geometry. The figure is not in scale. All the quantities are in milimeters.

As for the detectors, a stationary PLC mounted at an angle of 30° about 2 m from the neutron target was used to monitor the neutron yield throughout the entire experiment. Regarding the gamma production, a $CeBr_3$ detector was used as gamma monitor, placed 1 m away and at an angle of 110° from the end of the beam line.

Neutron spectra were measured by TOF technique using a ^{6}Li-glass detector [48]. The ^{6}Li-glass detector was 12.7 mm thick and had the geometry shown in Fig. 4. This detector was mounted on a movable arm that can rotate around the neutron target, covering an angular range from 0° and 90° in steps of 10°. The intrinsic efficiency of ^{6}Li-glass detector, shown in Fig. 5, is primarily defined by the ^{6}Li(n,t)^{4}He reaction, and it was determined by means of Monte Carlo (MC) simulations. The MCNP6.2 code [49] was employed for these calculations.

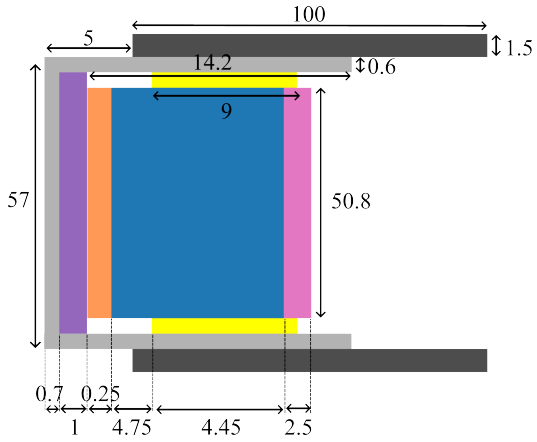

FIG. 4. ^{6}Li-glass detector geometry purchased from Scionix [48]. The colors represent the different materials: aluminum can (light grey), Si rubber (purple), Teflon layer (orange), ^{6}Li-Glass (blue), photomultiplier tube (pink), μ-metal (deep grey), and tape (yellow, between the Al can and the ^{6}Li-glass). All quantities are in millimeters; dimensions in figure are not to scale.

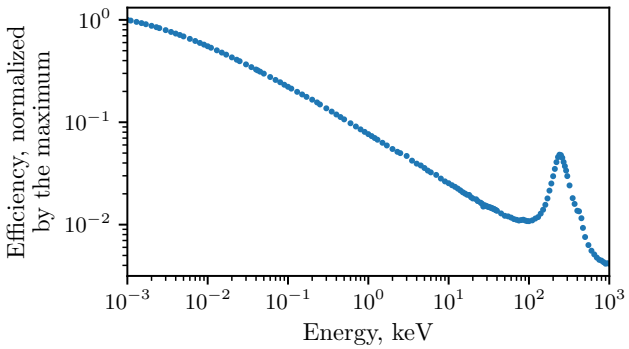

FIG. 5. Intrinsic efficiency for a 12.7 mm thick ^{6}Li-glass detector scaled to the maximum. Calculated by MC simulations using the geometry of the Figure 4.

The ABCD framework [50–53], maintained by the MONNET team [54], served as the front end for the Data Acquisition System (DAQ) in this experiment. ABCD is responsible for initializing the DAQ, reading the data from the hardware, storing, and processing the acquired waveforms. For our setup, we used the CAEN waveform digitizer model DT5730 [55], a desktop module that operates as the DAQ. The DT5730 features 8 channels with flash ADCs of 14 bit and 500 MSamples/s, making it suitable for high-resolution signal acquisition.

During data acquisition, signals collected at the anode of each detector were digitized and analysed using digital pulse-analysis routines. The waveforms analysis was applied to the digitized waveform to determine: the

energy, pulse shape, and time information of each waveform. Timing analysis utilized a digital timing filter amplifier and a constant-fraction discriminator to determine the precise timing of the signals. The time information is represented by a timestamp associated to each waveform. Pulse shape analysis is based on the double integration window technique [52]. Two parameters are determined: Qlong and Qshort. The former represents the total charge accumulated over an extended duration of the signal pulse, while Qshort corresponds to the charge within a shorter interval, typically near the peak of the pulse. The TOF information is determined with the differences between the timestamps and the signal driving the accelerator pulsing. Data from each detector were recorded independently, ensuring accurate alignment of timing and pulse integral information.

III. DATA ANALYSIS

In this section we detail the three measurements performed. The goal is the determination of the neutron spectrum of the ^{51}V(p,n)^{51}Cr reaction at E_p=1585 keV, i.e. 20 keV above the threshold. For this, two additional measurements with LiF target as neutron source were carried out. The first one was the measurement of the neutron field produced by the ^{7}Li(p,n)^{7}Be reaction near the threshold to validate setup and data analysis. The second one was a neutron transmission measurement through the Vanadium target using the measured neutron field produced by the ^{7}Li(p,n)^{7}Be reaction. This measurement was necessary to correct for the neutron absorption in the Vanadium target (500 μm in thickness) during the measurement at E_p=1585 keV.

A. Neutron spectra data analysis

The data analysis of all neutron spectra is determined by the TOF-to-energy conversion. The TOF for a given energy varies due to the potential different paths between the production point in the target and the final point inside the detector where the ^{6}Li(n,t)^{4}He reaction takes place. In this scenario, neutrons undergo multiple scattering events dependent on their energy and the materials they pass through. Consequently, for a neutron of a given energy, the resulting TOF forms a distribution [56, 57]. Therefore, the conversion TOF-to-energy is characteristic of each setup. The conversion cannot be measured directly. Thus, in neutron TOF experiments is conventionally obtained with accurate MC simulations. Hence, for a correct TOF-to-energy conversion, we carefully simulate with MCNP6.2 the complete setup. This includes modeling the neutron source as time-dependent Gaussian distribution with FWHM = 2 ns. Figure 6 shows the results of such simulations or response matrix (RM) for one of the cases, specifically, for Vanadium target with a flight path of 31 cm for the ^{6}Li-glass detector located at 0 degrees. The binning used is extracted by considering a temporal binning of 2 ns and transforming it to energy through the kinematic equation. Thus, the energy binning is not constant and we will call it "natural" binning.

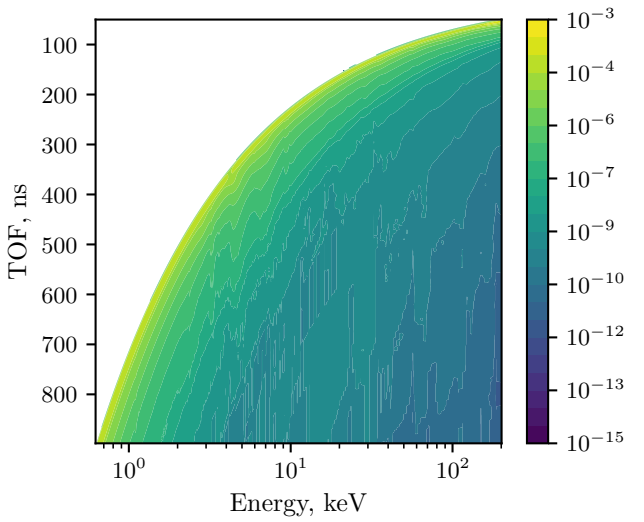

FIG. 6. Response matrix using Vanadium target and ^{6}Li-glass detector at 31 cm and 0 degrees. As explained in the text, dedicated response matrices are calculated for the different cases.

B. ^{7}Li(p,n)^{7}Be near threshold

The ^{7}Li(p,n)^{7}Be is a very well-known reaction near threshold with several experimental dataset, see [58] and references therein, and very accurate theoretical parametrization [59]. In particular, the neutron field produced at E_p=1912 keV and measured in 1988 by Ratynski and Käppeler, i.e. about 30 keV above the reaction threshold, is considered an standard [12, 56, 57, 60, 61].

Therefore, the ^{7}Li(p,n)^{7}Be reaction near threshold can be used for validation of the setup and data analysis [57]. Our measurement began by checking the ^{7}Li(p,n)^{7}Be reaction threshold to validate the accelerator calibration. The calibration has an uncertainty of 2 keV, and at proton energy of E_p=1888.5 keV neutrons were clearly detected, meanwhile, going down in energy, no neutrons were detected at E_p=1884.6 keV. Therefore, an energy of (-4 $\pm$ 2) keV was added to the calibrated accelerator energy, because the threshold ^{7}Li(p,n)^{7}Be reaction is expected at E_p=1880.6 keV. Due to technical reasons for optimal terminal stability, the accelerator was finally settled at E_p=(1915 $\pm$ 4) keV. The ^{6}Li-glass detector was placed at 31 cm away from the neutron-production target and at an angle of 0 degrees with respected to the proton-beam axis. A charge of 4015.35 μA/Hz was applied, with a total measurement time of 91.15 minutes. Using the reference channel from the accelerator pulse,

Figure 7 (upper part) displays a TOF histogram for a ^{6}Li-glass detector.

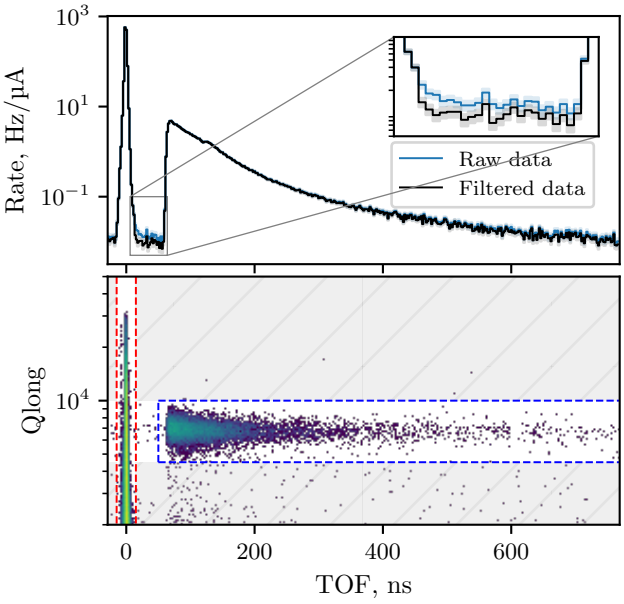

FIG. 7. Time-Of-Flight spectrum for raw and filtered data from the measurement of the ^{7}Li(p,n)^{7}Be reaction at E_p=(1915 ± 4) keV, taken at a distance of 31 cm and at 0 degrees. The upper section presents a zoomed-in view of the flat region of the spectra. The lower section shows a representation of the Qlong distribution.

As we can see in the zoom-in of the upper part of the Fig. 7, the background was found to be temporally uniform since the region between the gamma-flash and the neutrons was flat. This allows its subtraction from the measured TOF spectra. An additional analysis in function of the Qlong allows a discrimination between the gamma-rays and neutrons. The region of interest for the neutrons for this detector is outlined by the dotted blue lines in Fig. 7. By isolating the signal attributed to neutrons and excluding gamma-rays within the neutron range, the resulting spectrum is showed by the black line in the upper part of Figure 7. This reaffirms that the background was completely flat.

For the TOF-to-energy conversion, we use the corresponding response matrix. As uncertainty is mainly dominated by statistics, once the TOF is transformed to "natural" energy grid, the histograms are rebinned to 2 keV bins as a good compromise between resolution and low uncertainty. Figure 8 shows our results at 0° compared to those of Lederer *et al.* [60] measured at E_p=(1910 ± 1) keV, Feinberg *et al.* [61] measured at E_p=(1913 ± 6) keV and Macías *et al.* measured at E_p=(1912 ± 2). Despite the differences in proton energies between the different experiments, the comparison demonstrate the consistency of our acquisition system and data analysis. The final uncertainties are shown as error bars. The most significant source is statistical, the one related to the simulations of response matrix contribute less than 1%.

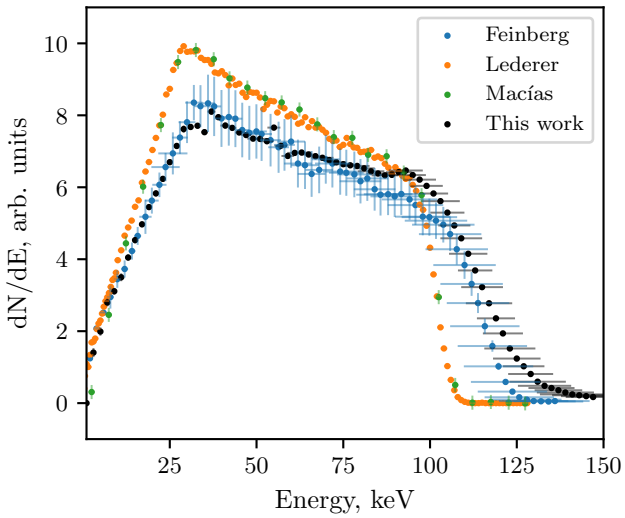

FIG. 8. Energy spectrum at 0 degrees of the ^{7}Li(p,n)^{7}Be at E_p=(1915 ± 4) keV, with its statistical uncertainty, compared with Lederer *et al.* at E_p=(1910 ± 1) keV [60], Feinberg *et al.* at E_p=(1913 ± 6) keV [61] and Macías *et al.* at E_p=(1912 ± 2) keV [56].

An important aspect of our investigation is the normalization because our primary goal is to validate the method and subsequently use it to normalize the neutron yield from the Vanadium reaction. For the lithium energy spectrum measured at a distance of 31 cm, we observed a production rate of (1533 ± 22) neutrons in arbitrary units within the energy range from 1 to 150 keV. This high production rate indicates a robust reaction yield at closer proximity to the detector.

The data collected will serve as a reference to normalize the neutron yield of the vanadium reaction, ensuring that our results are accurate and reliable. At the energy of 1910 keV the total neutron yield using a thick LiF target is 7.29×10^6 neutrons×Hz/μA, following Ref. [59]. Using NEBOAS [62, 63], we have determined that the neutron rate spectrum at a distance of 31 cm amounts to 1.43×10^5 neutrons×Hz/μA for an initial proton energy of E_p=1915 keV. This value will be used to standardize the neutron yield for the vanadium reaction.

C. Transmission through Vanadium target

Due to the thickness of the Vanadium target, the neutron self-absorption would be appreciable. For correcting the absorption, a transmission TOF measurement was performed using the previous measured neutron field. Figure 9 details the setup where a Vanadium foil with a thickness of 0.5 mm was placed at 12 cm from the LiF target.

Using the presented method to transform TOF into energy, in the Fig. 10, we show the energy spectra difference

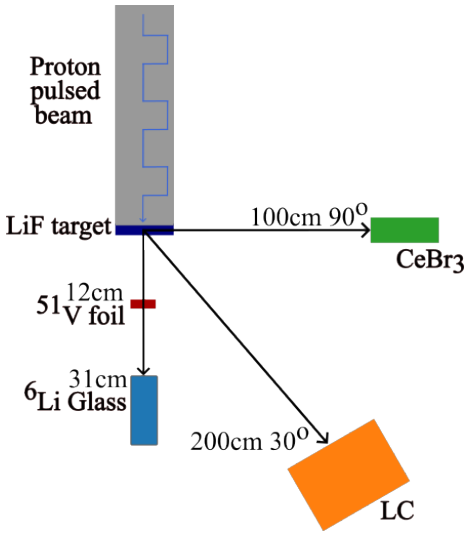

FIG. 9. Setup for the neutron vanadium transmission measurement. All the quantities are in cm and the figure is not in scale.

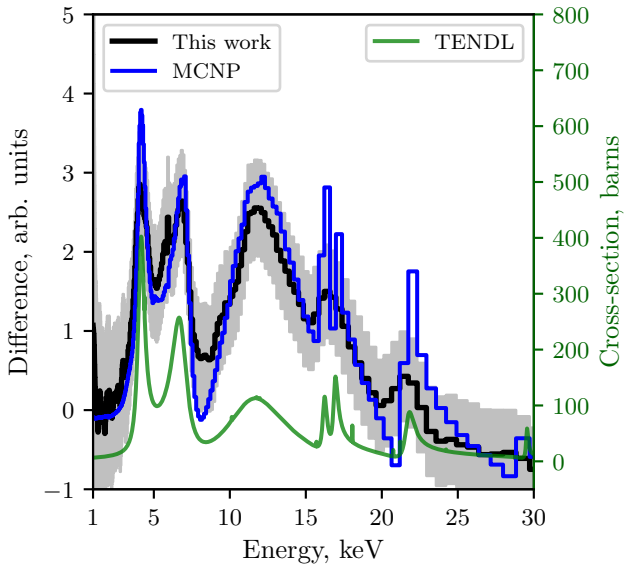

FIG. 10. Black line - Difference between the two energy spectra with and without Vanadium. Grey shadow - Error of the difference between the two spectra with and without Vanadium. Green line - ^{51}V(n,tot) TENDL [44] cross-section. Blue line - Difference between the two spectra with and without Vanadium results from MCNP6.2 simulations. Simulations were run for a sufficient duration until the errors became negligible.

between the measurement with Vanadium and without Vanadium (black line) in the energy range of interest for the measurement. The gray shadow represent the experimental uncertainty of the difference. The calculated difference from MCNP6.2 [49] simulations is shown in blue. In these simulations, we modeled the experimental conditions with and without vanadium, then subtracted the resulting neutron spectra to obtain the difference. The initial neutron spectrum used for these simulations was the angle-dependent spectrum for ^{7}Li(p,n) at E_p=1915 keV, obtained by a code based on Lee and Zhou's equations [59]. This code was successfully compared with experimental data [64, 65]. Additionally, we show the ^{51}V(n,tot) TENDL [44] cross-section in green, to evaluate whether the effect aligns with our expectations.

In Figure 10 there is a strong agreement between the experimental and simulated results, particularly in the energy resonances, which are identified with high resolution. However, the most significant aspect of the figures is not just the agreement in numerical values, but the fact that the overall shape of the experimental and simulated differences closely mirrors one another. The experimental data, much like the simulation, reveals five distinct and clearly defined peaks, which are consistent with the structure observed in the represented TENDL cross-section. This consistency between the shape suggests that, despite any minor quantitative discrepancies, the simulation successfully reproduces the key features of the experimental results, particularly the positions and relative heights of the energy resonances. This will allow the correction of absorption in the target in the Vanadium target for the different angles.

D. ^{51}V(p,n)^{51}Cr at E_p=1585 keV

Our goal measurement with vanadium have followed the same data analysis as presented above. All the ^{51}V(p,n) TOFs measurements were conducted using the same ^{6}Li-glass detector, positioned at 31 cm, with a period of 800 ns at E_p (1585±2) keV. Figure 11 shows the TOF histogram at zero degrees, which reveals the presence of several resonances. In the next section, the results in energy for all the angles are detailed.

IV. RESULTS AND DISCUSSION

As above, the TOFs have been convert into energy spectrum, following the validate method explained in Section II. The obtained energy spectra for the different angles are shown in Figure 12. The binning employed here is the "natural" energy binning and the energy range spans from 1 to 30 keV.

Specifically, for the measurement taken at 0 degrees, we convert the TOF data presented in Fig. 11 into the energy spectrum using the response matrix illustrated in Fig. 6. The response matrix was constructed using the validated MCNP6.2 code with the TENDL cross-section for the V(n,tot) reaction. Transmission measurements confirmed that the code accurately represents the V(n,tot) resonances for each scenario.

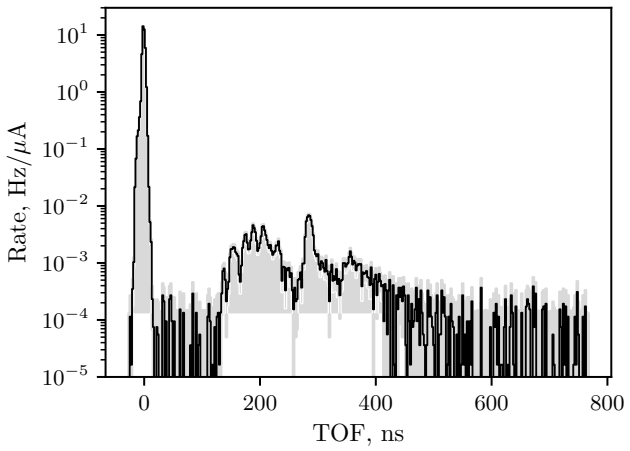

FIG. 11. Time-Of-Flight measurement for the ^{51}V(p,n)^{51}Cr at E$_p$=(1585 ± 2) keV, just 20 keV above the threshold, at zero degrees. The grey shadow represents the statistical error of the measure.

As mentioned, we have created dedicated response matrices for each angle for taking into account the specific thickness of vanadium that the neutrons pass through. This ensures that the energy spectra derived from the TOF data accurately represent the effects of neutron interactions with the Vanadium target at various angles. Thus, the resonances we see in Figure 12 are resonances from the ^{51}V(p,n) reaction itself, not from secondary reactions.

In Figure 12 the resonances for each angle are marked in blue lines, it is clear that these resonances are changing depending on the angle. The main resonances marked in dark blue lines are in agreement with the 6.44 ± 0.195 resonance peak at 0 degrees measured by Schölermann and Böttger [24] and confirmed by Lamirand [26].

By comparing these results with those obtained from the ^{7}Li(p,n) reaction measurements, we can determine a ratio of production between them. Notably, the zero-degree measurement, depicted in Figure 12 at the upper left, was conducted under identical conditions as the one taken at 0° using a ^{6}Li-glass detector positioned at 31 cm. This allows for a direct comparison between the two spectra. The calculated ratio of production between the two reactions is 1944.8 at zero degrees, indicating a significant comparative difference in reaction yields under these specific experimental conditions. Using the value for the ^{7}Li(p,n) reaction at 31 cm of 1.43×10^5 neutrons×Hz/μA, we can use it to normalize.

To obtain the neutron spectrum at the production target, angle-integrated neutron spectra are needed. For this, each spectrum is scaled by the respective covered solid angle. We are going to follow this criteria:

$$f_\alpha = \begin{cases} 2\pi\left(1 - cos(\theta)\right) & \text{if } \alpha = 0. \\ 2\pi\left(cos(\alpha-\theta) - cos(\alpha+\theta)\right), & \text{if } 0 > \alpha > 90. \\ 2\pi\left(cos(90-\theta)\right), & \text{if } \alpha = 90. \end{cases} \tag{1}$$

Where r is the detector radius, α is the position degree of the detector and θ is the covered degree by the detector, calculated by:

$$\theta = arctan\left(\frac{r}{L}\right), \tag{2}$$

using L as flight path.

The pondered spectra for each angle is shown in Fig. 13. For the present setup, with detectors of 5.08 cm diameter and a flight path of 31 cm, the entire forward hemisphere is narrowly avoided. Nevertheless, previous studies by other researchers have investigated potential variations in the angle-integrated spectrum for the ^{7}Li(p,n) reaction at a proton energy of 1912 keV [56, 60] showing a negligible effect.

In Figure 14 the integrated spectrum for the ^{51}V(p,n)^{51}Cr reaction is shown. The result is obtained by adding all the angle-degree dependence spectrum from the Fig. 13 and normalizing using the ^{7}Li(p,n) neutron yield. The black line represent the spectrum with the "natural" binning, extracted from the 2 ns steps in time. The grey shadow is the statistical error. The most important contribution to the statistic uncertainty is due to the low statistics at the higher angles.

The shape of this energy spectrum is characteristic, because of the main resonance, which have been found in all the measured angles, in Fig. 12. The total forward neutron yield is (65000 ± 24000) neutrons×Hz×/μA for the ^{51}V(p,n) reaction at E$_p$=(1585 ± 2) keV.

V. CONCLUSIONS

The main objective of this work was to produce and measure the neutron spectrum with the ^{51}V(p,n)^{51}Cr reaction at E$_p$=1585 keV, that is 20 keV above the threshold. The experiment encompassed three measurements conducted at the MONNET facility at the Joint Research Centre in Geel, Belgium, using the Time-Of-Flight technique. One was the mentioned measurement of ^{51}V(p,n)^{51}Cr at 1585 keV. To validate the data acquisition and analysis, the well-known ^{7}Li(p,n)^{7}Be reaction near threshold was used. Then, with the latter measured neutron spectrum a transmission measurement through Vanadium was performed to correct for neutron absorption in the Vanadium target.

The forward integrated neutron spectrum of ^{51}V(p,n)^{51}Cr at 1585 keV, shown in Fig. 14, is clearly dominated by the presence of resonances. At a first glance the comparison with a stellar neutron spectrum at kT = 5 keV would show discrepancies. Nevertheless, in future works we will study possible

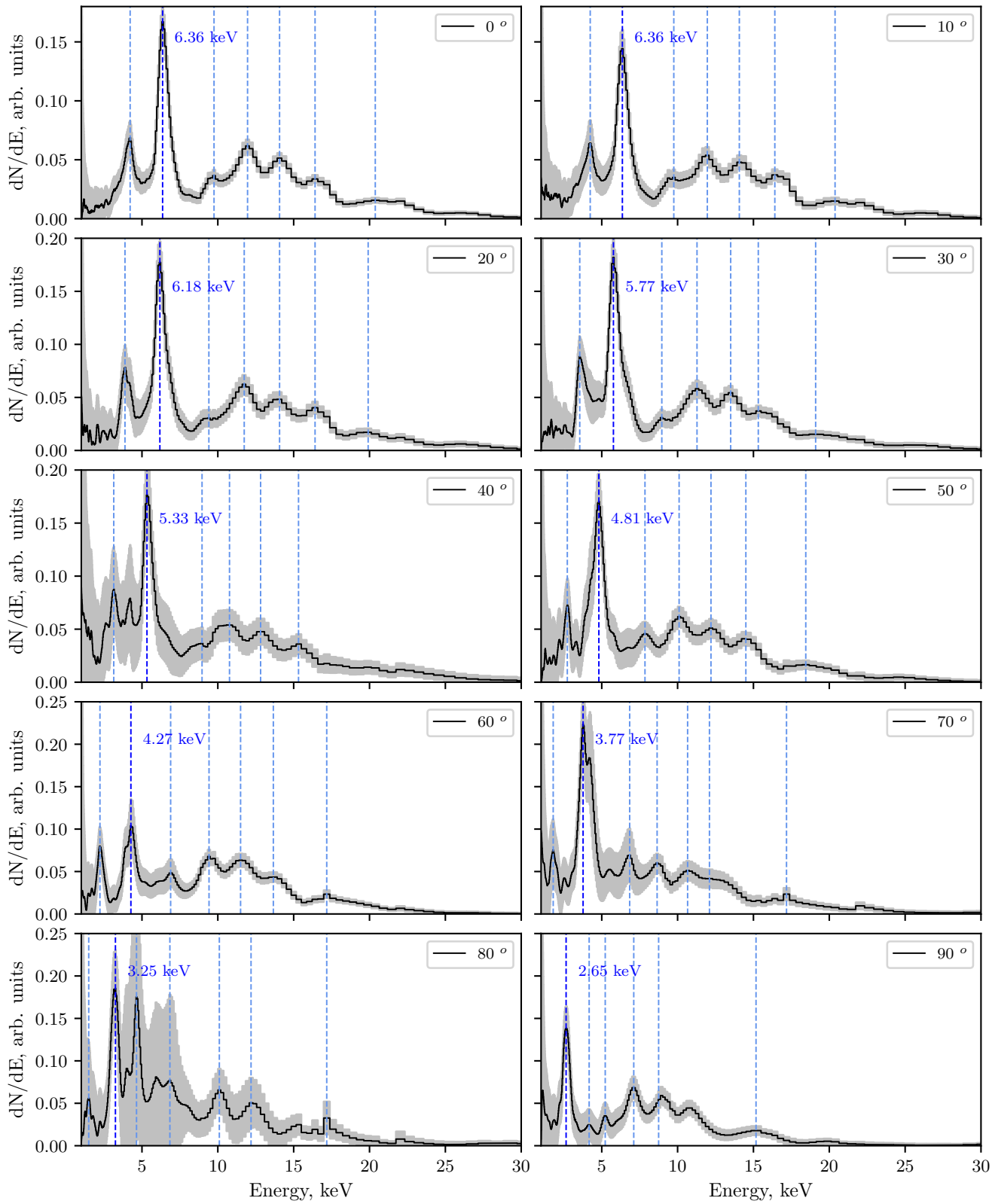

FIG. 12. Energy spectrum of ^{51}V(p,n)^{51}Cr at E_p=(1585 ± 2) keV for 10 different angles. The shadow grey indicate the statistical error. All the resonances are marked in dashed blue lines, and the main resonance for each angle is marked in dark blue dashed lines, and the energy value is annotated in for each graph.

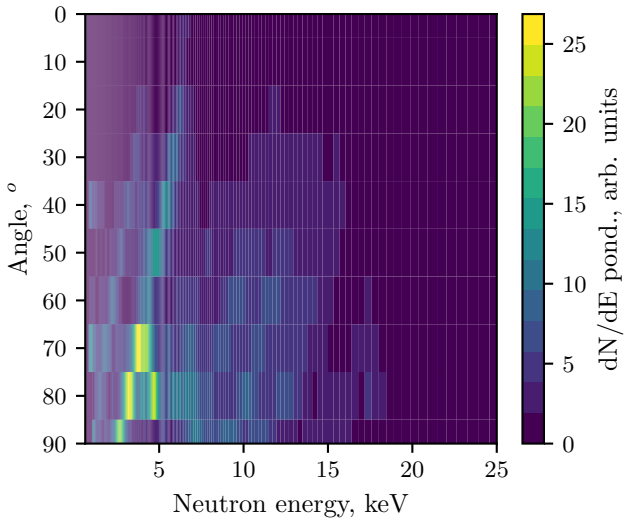

FIG. 13. Energy spectrum pondered by the solid angle of ^{51}V(p,n) reaction at (1585±2) keV for 10 different angles.

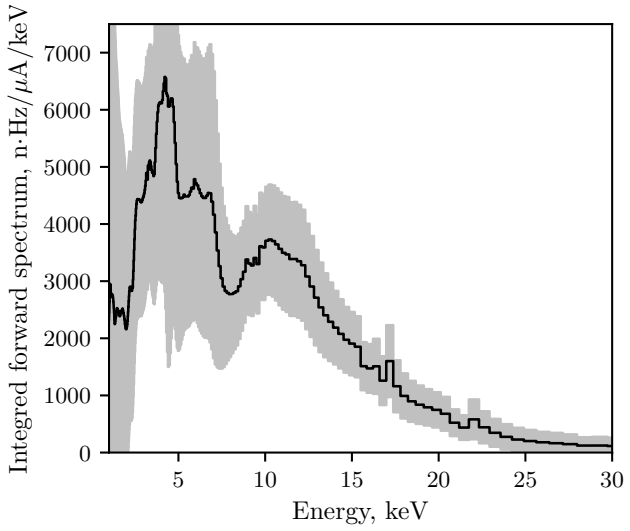

FIG. 14. Forward integrated energy spectrum for ^{51}V(p,n) at E_p=(1585 ± 2) keV.

ways of producing neutron fields closer to the stellar one using shaped proton beams following the methodology in previous studies with the ^{7}Li(p,n)^{7}Be, see [57] and references therein.

On the other hand, the neutron spectrum of Fig. 14 is very adequate for BNCT without neutron moderation, because most of the neutrons will have a therapeutic effect (energy between 0.25 eV and 10 keV). Nevertheless, we will perform carefully studies following the methodology in [17] to explore this possibility. It is worth mentioning that the low neutron yield of the reaction will entail the use of proton currents higher than delivered by existing accelerators.

ACKNOWLEDGMENTS

This work has been carried out within the framework of project PID2020.117969RB.I00 funded by MICIU/AEI /10.13039/5011000110 33. The beam line for the measurement plus an early-researcher stay of three months at JRC-Monnet for the PhD student, Antònia Verdera, have received funding from the Euratom research and training programme 2014-2018 undergrant agreement No 847594 (ARIEL) [66].

[1] A. O. Hanson, R. F. Taschek, and J. Williams, Monoergic neutrons from charged particle reactions, Reviews of Modern Physics **21**, 635 (1949).

[2] K. Harris, H. Grench, R. Johnson, and F. Vaughn, The ^{51}V(p,n)^{51}Cr reaction as a neutron source of known intensity, Nuclear Instruments and Methods **33**, 257 (1965).

[3] K. Harris, H. Grench, R. Johnson, F. Vaughn, J. Ferziger, and R. Sher, The ^{197}Au(n,γ)^{197}Au cross section from 13 keV to 683 keV, Nuclear Physics **69**, 37 (1965).

[4] J. Marion, R. Levesque, C. Ludemann, and R. Detenbeck, A Versatile, High Efficiency 4π Neutron Detector, Nuclear Instruments and Methods **8**, 297 (1960).

[5] H. Schmitt and C. Cook, Absolute neutron absorption cross sections for Sb-Be photoneutrons, Nuclear Physics **20**, 202 (1960).

[6] Y.-T. Li, W.-P. Lin, B.-S. Gao, H. Chen, H. Huang, Y. Huang, T.-Y. Jiao, K.-A. Li, X.-D. Tang, X.-Y. Wang, *et al.*, Development of a low-background neutron detector array, Nuclear Science and Techniques **33**, 41 (2022).

[7] E. M. Burbidge, G. R. Burbidge, W. A. Fowler, and F. Hoyle, Synthesis of the elements in stars, Rev. Mod. Phys. **29**, 547 (1957).

[8] A. G. W. Cameron, Nuclear reactions in stars and nucleogenesis, Publications of the Astronomical Society of the Pacific **69**, 201 (1957).

[9] M. Lugaro, F. Herwig, J. C. Lattanzio, R. Gallino, and O. Straniero, s-process nucleosynthesis in asymptotic giant branch stars: A test for stellar evolution, The Astrophysical Journal **586**, 1305 (2003).

[10] R. Gallino, C. Arlandini, M. Busso, M. Lugaro, C. Travaglio, O. Straniero, A. Chieffi, and M. Limongi, Evolution and Nucleosynthesis in Low-Mass Asymptotic Giant Branch Stars. II. Neutron Capture and the s-Process, The Astrophysical Journal **497**, 388 (1998).

[11] T. Rauscher, P. Mohr, I. Dillmann, and R. Plag, Opportunities to constrain astrophysical reaction rates for s-process via determination of the ground-state cross-sections, The Astrophysical Journal **738**, 143 (2011).

[12] W. Ratynski and F. Käppeler, Neutron capture cross section of ^{197}Au: A standard for stellar nucleosynthesis, Phys. Rev. C **37**, 595 (1988).

[13] R. Reifarth, P. Erbacher, S. Fiebiger, *et al.*, Neutron-induced cross sections, European Physical Journal Plus **133**, 424 (2018).

[14] M. Heil, S. Dababneh, A. Juseviciute, F. Käppeler, R. Plag, R. Reifarth, and S. O'Brien, Quasistellar spectrum for neutron activation measurements at kT = 5 keV, Phys. Rev. C **71**, 025803 (2005).

[15] W. H. Jin, C. Seldon, M. Butkus, W. Sauerwein, and H. B. Giap, A Review of Boron Neutron Capture Therapy: Its History and Current Challenges, International journal of particle therapy **9**, 71 (2022).

[16] IAEA., *Advances in Boron Neutron Capture Therapy*, Non-serial Publications (International Atomic Energy Agency, Vienna, 2023).

[17] A. Verdera and J. Praena, Study on novel neutron irradiation without beam shaping assembly in Boron Neutron Capture Therapy, Scientific Reports **14**, 22434 (2024).

[18] R. Smith and H. Richards, Proton-neutron thresholds in V-51 and Mn-55, in *Physical Review*, Vol. 74 (American Physical Soc One Physics Ellipse, College PK, MD 20740-3844 USA, 1948) pp. 1257–1257.

[19] H. T. Richards, R. V. Smith, and C. P. Browne, Proton-Neutron Reactions and Thresholds, Phys. Rev. **80**, 524 (1950).

[20] J. Gibbons, R. Macklin, and H. Schmitt, ^{51}V(p,n)^{51}Cr Reaction as a 5-to 120-keV Neutron Source, Physical Review **100**, 167 (1955).

[21] C. R. Gossett and J. W. Butler, Neutron Thresholds in the ^{51}V(p,n)^{51}Cr, ^{55}Mn(p,n)^{55}Fe, ^{70}Zn(p,n)^{70}Ga, and ^{75}As(p,n)^{75}Se Reactions, Phys. Rev. **113**, 246 (1959).

[22] C. Johnson, C. Trail, and A. Galonsky, Thresholds for (p,n) reactions on 26 intermediate - weight nuclei, Physical Review **136**, 1719 (1964).

[23] D. W. Kneff, H. W. Lefevre, and G. U. Din, Reaction Q Values from Near-Threshold Neutron Spectra, Phys. Rev. Lett. **25**, 1210 (1970).

[24] H. Scholermann and R. Bottger, Q-values for (p, n) reactions on 65cu and 51v, Nuclear Physics A **501**, 86 (1989).

[25] P. Stelson, W. Preston, and C. Goodman, The v 51 (p, n) cr 51 neutron spectrum, Physical Review **80**, 287 (1950).

[26] V. Lamirand, *Determination of cross sections for the production of low-energy monoenergetic neutron fields*, Ph.D. thesis, Université de Grenoble (2011).

[27] R. Ballini, Y. Cassagnou, C. Levi, and L. Papineau, Spectrometry of time-of-flight of neutrons from the (p,n) reaction on vanadium, Compt. rend. **251** (1960).

[28] G. Deconninck and J. Royen, La reaction ^{51}V(p,n)^{51}Cr comme source de neutrons monoenergetiques, Nuclear Instruments and Methods **75**, 266 (1969).

[29] C. Johnson, A. Galonsky, and J. Ulrich, Proton strength functions from (p,n) cross sections, Physical Review **109**, 1243 (1958).

[30] R. D. Albert, (p,n) cross section and proton optical-model parameters in the 4- to 5.5-MeV energy region, Phys. Rev. **115**, 925 (1959).

[31] J. Wing and J. R. Huizenga, (p, n) Cross Sections of ^{51}V, ^{52}Cr, ^{63}Cu, ^{65}Cu,^{107}Ag, ^{109}Ag, ^{11}Cd, ^{114}Cd, and^{139}La from 5 to 10.5 mev, Phys. Rev. **128**, 280 (1962).

[32] S. Hontzeas and L. Yaffe, Interaction of vanadium with protons of energies up to 84 MeV, Canadian Journal of Chemistry **41**, 2194 (1963).

[33] G. F. Dell, W. D. Ploughe, and H. J. Hausman, Total Reaction Cross Sections in the Mass Range 45 to 65, Nuclear Physics **64**, 513 (1965).

[34] J. J. Egan, K. K. Sekharan, G. C. Dutt, J. E. Wiest, and F. Gabbard, 2.335-MeV isobaric analog resonance in ^{51}V+p and the excited states of ^{51}Cr studied via the (p,n) and $(p, n\gamma)$ Reactions, Phys. Rev. C **5**, 1562 (1972).

[35] K. Sekharan and M. K. Mehta, Absolute reaction cross section of the reaction ^{51}V(p,n)^{51}Cr over the isobaric analog resonance near 2.340 MeV, Physical Review C **6**, 2304 (1972).

[36] M. Mehta, S. Kailas, and K. Sekharan, Total (p,n) reaction cross section study on ^{51}V over the incident energy range 1· 56 to 5· 53 mev, Pramana **9**, 419 (1977).

[37] L. Mitchell, M. Anderson, S. Kennett, and D. Sargood, Cross Sections and Thermonuclear Reaction Rates for ^{42}Ca(p,γ)^{43}Sc,^{44}Ca$(p,\gamma)^{45}$Sc,^{44}Ca$(p,n)^{44}$Sc and ^{45}Sc$(p,n)^{45}$Ti, Nuclear Physics A **380**, 318 (1982).

[38] J. Zyskind, C. Barnes, J. Davidson, W. A. Fowler, R. Marrs, and M. Shapiro, Competition effects in proton-induced reactions on ^{51}V, Nuclear Physics A **343**, 295 (1980).

[39] S. Kailas, S. Gupta, S. Kerekatte, and C. Fernandes, 51 (p, n) 51 cr reaction from e p 1.9 to 4.5 mev, Pramana **24**, 629 (1985).

[40] Z. Wenrong, L. Hanlin, and Y. Weixiang, Excitation function of V-51(p, n)Cr-51 up to 22 MeV, Chin J Nucl Phys **16**, 67 (1994).

[41] M. Musthafa, M. Kumar Sharma, B. Singh, and R. Prasad, Measurement and analysis of cross sections for (p,n) reactions in ^{51}V and ^{113}In, Applied Radiation and Isotopes **62**, 419 (2005).

[42] A. Solieman, M. Al-Abyad, F. Ditroi, and Z. Saleh, Experimental and theoretical study for the production of ^{51}Cr using p, d, ^{3}He and ^{4}He projectiles on v, ti and cr targets, Nuclear Instruments and Methods in Physics Research Section B: Beam Interactions with Materials and Atoms **366**, 19 (2016).

[43] N. Otuka, E. Dupont, V. Semkova, B. Pritychenko, A. Blokhin, M. Aikawa, S. Babykina, M. Bossant, G. Chen, S. Dunaeva, R. Forrest, T. Fukahori, N. Furutachi, S. Ganesan, Z. Ge, O. Gritzay, M. Herman, S. Hlavač, K. Katō, B. Lalremruata, Y. Lee, A. Makinaga, K. Matsumoto, M. Mikhaylyukova, G. Pikulina, V. Pronyaev, A. Saxena, O. Schwerer, S. Simakov, N. Soppera, R. Suzuki, S. Takács, X. Tao, S. Taova, F. Tárkányi, V. Varlamov, J. Wang, S. Yang, V. Zerkin, and Y. Zhuang, Towards a more complete and accurate experimental nuclear reaction data library (exfor): International collaboration between nuclear reaction data centres (nrdc), Nuclear Data Sheets **120**, 272 (2014).

[44] A. Koning, D. Rochman, J.-C. Sublet, N. Dzysiuk, M. Fleming, and S. van der Marck, TENDL: Complete Nuclear Data Library for Innovative Nuclear Science and Technology, Nuclear Data Sheets **155**, 1 (2019), special Issue on Nuclear Reaction Data.

[45] R. Michel and G. Brinkmann, Depth-dependent production of radionuclides (44 ¡= a¡= 59) by solar protons in extraterrestrial matter.[200 mev proton reactions with ni, fe, mn, cr, and ti], J. Radioanal. Chem.;(Switzerland) **59** (1980).

[46] C. L. Fontana, B. Cédric, W. Geerts, M. M. Martinez, M. Vidali, and S. Oberstedt, JRC MONNET - the intense fast-neutron source for fundamental and application-driven research, in *EPJ Web of Conferences*, Vol. 284 (EDP Sciences, 2023) p. 06002.

[47] A. Seibert, L. A. de las Heras, K. Boboridis, E. Colineau, R. Eloirdi, C. L. Fontana, M. Hult, A. Jenet, E. Michailidou, K.-F. Nilsson, *et al.*, The nuclear research infrastructures open access scheme of the Joint Research Centre (JRC) at the European Commission–Contributions to education, training, mobility and scientific excellence, Nuclear Engineering and Design **420**, 113000 (2024).

[48] SCIONIX, SCIONIX - Dedicated Scintillation Detectors, https://scionix.nl.

[49] C. J. Werner, J. S. Bull, C. J. Solomon, F. B. Brown, G. W. McKinney, M. E. Rising, D. A. Dixon, R. L. Martz, H. G. Hughes, L. J. Cox, A. J. Zukaitis, J. C. Armstrong, R. A. Forster, and L. Casswell, *MCNP6.2 Release Notes - report LA-UR-18-20808* (Los Alamos National Laboratory (LANL), 2018).

[50] C. L. Fontana, M. Lunardon, F. E. Pino, L. Stevanato, A. Carnera, C. Sada, F. Soramel, and S. Moretto, A distributed data acquisition system for signal digitizers with on-line analysis capabilities, in *2017 IEEE Nuclear Science Symposium and Medical Imaging Conference (NSS/MIC)* (IEEE, 2017) pp. 1–5.

[51] C. L. Fontana, M. Lunardon, F. Pino, L. Stevanato, and S. Moretto, Resource sharing in nuclear physics laboratory classes: A distributed data acquisition system for experiments with shared resources and data management, in *25th International Conference on the Application of Accelerators in Research and Industry (CAARI)* (AIP Publishing, Texas, USA, 2019) p. 050024.

[52] C. L. Fontana, N. Tuccori, F. E. Pino, M. Lunardon, L. Stevanato, and S. Moretto, Performance comparison between signal digitizers and low-cost digital oscilloscopes: spectroscopic, pulse shape discrimination and timing capabilities for nuclear detectors, Journal of Instrumentation **15** (06), P06020.

[53] F. Pino, C. L. Fontana, G. Nebbia, B. Pedersen, G. Varasano, A. Sardet, C. Carasco, B. Pérot, A. G. Sebert, J.-P. Poli, *et al.*, Performance evaluation of a new digital acquisition system for neutron detection and spectroscopy, Nuclear Instruments and Methods in Physics Research Section A: Accelerators, Spectrometers, Detectors and Associated Equipment , 164743 (2020).

[54] J. R. C. European Commission, Github - ABCD, https://github.com/ec-jrc/abcd/.

[55] CAEN SpA, *User Manual UM3148 DT5730 / DT5725*, CAEN SpA (2016), available from `https://www.caen.it/products/dt5730/`.

[56] M. Macías, B. Fernández, and J. Praena, The first neutron time-of-flight line in spain: Commissioning and new data for the definition of a neutron standard field, Radiation Physics and Chemistry **168**, 108538 (2020).

[57] J. Praena, A. Verdera, J. G. López, and G. Martín-Hernández, Production and measurement of a stellar neutron spectrum at 30 keV, The European Physical Journal A **60**, 199 (2024).

[58] G. Martín-Hernández, P. Mastinu, M. Maggiore, L. Pranovi, G. Prete, J. Praena, R. Capote-Noy, F. Gramegna, A. Lombardi, L. Maran, C. Scian, and E. Munaron, Excitation function shape and neutron spectrum of the ^{7}Li$(p,n)^{7}$Be reaction near threshold, Phys. Rev. C **94**, 034620 (2016).

[59] C. Lee and X.-L. Zhou, Thick target neutron yields for the 7li(p,n)7be reaction near threshold, Nuclear Instruments and Methods in Physics Research Section B: Beam Interactions with Materials and Atoms **152**, 1 (1999).

[60] C. Lederer, F. Käppeler, M. Mosconi, R. Nolte, M. Heil, R. Reifarth, S. Schmidt, I. Dillmann, U. Giesen, A. Mengoni, and A. Wallner, Definition of a standard neutron field with the ^{7}li$(p,n)^{7}$be reaction, Phys. Rev. C **85**, 055809 (2012).

[61] G. Feinberg, M. Friedman, A. Krása, A. Shor, Y. Eisen, D. Berkovits, D. Cohen, G. Giorginis, T. Hirsh, M. Paul, A. J. M. Plompen, and E. Tsuk, Quasi-stellar neutrons from the ^{7}li$(p,n)^{7}$be reaction with an energy-broadened proton beam, Phys. Rev. C **85**, 055810 (2012).

[62] M. Macias, Neboas project. joint research centre. european commission., https://code.europa.eu/neboas.

[63] M. Macías, C. Bonaldi, C. Fontana, W. Geerts, A. Plompen, S. Oberstedt, and M. Vidali, NEBOAS: a Neutron yiElds Based On AcceleratorS application, Computer Physics Communications , 109304 (2024).

[64] J. Praena, P. Mastinu, M. Pignatari, J. Quesada, J. García-López, M. Lozano, N. Dzysiuk, R. Capote, and G. Martín-Hernández, Measurement of the MACS of ^{181}Ta(n,γ) at kT=30keV as a test of a method for Maxwellian neutron spectra generation, Nuclear Instruments and Methods in Physics Research Section A: Accelerators, Spectrometers, Detectors and Associated Equipment **727**, 1 (2013).

[65] J. Praena, P. Mastinu, M. Pignatari, J. Quesada, R. Capote, and Y. Morilla, Measurement of the MACS of ^{159}Tb(n,γ) at kT=30 keV by Activation, Nuclear Data Sheets **120**, 205 (2014).

[66] A. H2020, Ariel project (2020), accessed: 2024-06-06.